OPEN ACCESS



Devouring the Centaurus A Satellites: Modeling Dwarf Galaxies with Galacticus

Sachi Weerasooriya^{1,2}, Mia Sauda Bovill^{1,3}, Matthew A. Taylor⁴, Andrew J. Benson², and Cameron Leahy⁴, Department of Physics and Astronomy, Texas Christian University, Fort Worth, TX 76109, USA² The Observatories of the Carnegie Institution for Science, 813 Santa Barbara Street, Pasadena, CA 91101, USA; sweerasooriya@carnegiescience.edu

³ Department of Astronomy, University of Maryland, College Park, MD 20742, USA

⁴ University of Calgary, 2500 University Drive NW, Calgary Alberta T2N 1N4, Canada

**Received 2023 August 21: revised 2024 March 18: accepted 2024 March 25: published 2024 June 12

Abstract

For the first time, systematic studies of dwarf galaxies are being conducted throughout the Local Volume, including the dwarf satellites of the nearby giant elliptical galaxy Centaurus A (NGC 5128). Given Centaurus A's mass (roughly 10 times larger than that of the Milky Way), AGN activity, and recent major mergers, investigating the dwarf galaxies of Centaurus A and their star formation physics is imperative. However, simulating the faintest dwarfs around a galaxy of Centaurus A's mass with sufficient resolution in a hydrodynamic simulation is computationally expensive and currently infeasible. In this study, we seek to reproduce the properties of Centaurus A dwarfs using the semianalytic model GALACTICUS to model dwarfs within a 700 kpc region around Centaurus A, corresponding approximately to its splashback radius. We investigate the effects of host halo mass and environment and predict observable properties of Centaurus A dwarfs using astrophysical prescriptions and parameters previously tuned to match properties of the Milky Way's satellite galaxies. This approach allows us to approximately replicate cumulative luminosity functions, and luminosity-metallicity and luminosity-half-lightradii relations observed in the Centaurus A satellites. We provide predictions for the velocity dispersions, and star formation histories of Centaurus A dwarfs. The agreement between our predicted star formation histories for Centaurus A dwarfs and those of the Milky Way dwarfs implies the presence of universal processes governing star formation in dwarf galaxies. Overall, our findings shed light on the star formation physics of dwarf galaxies in the Centaurus A system, revealing insights into their properties and dependence on the host environment.

Unified Astronomy Thesaurus concepts: Galaxy evolution (594); N-body simulations (1083); Dwarf galaxies (416); Galaxy formation (595)

Supporting material: machine-readable table

1. Introduction

Dwarf galaxies are the fundamental building blocks of larger structures. They are the most abundant type of galaxies in the Universe at all redshifts (e.g., Binggeli et al. 1988; Ferguson & Binggeli 1994; Marzke & da Costa 1997), and the dwarf galaxies of the Local Group are well studied both observationally (McConnachie 2012; York et al. 2012; Martin et al. 2016; Albareti et al. 2017; Abbott et al. 2018; Aguado et al. 2019) and theoretically (Hopkins et al. 2018; Pandya et al. 2020; Applebaum et al. 2021; Shipp et al. 2023; Weerasooriya et al. 2023).

The shallow gravitational potential wells of dwarf galaxies make them extremely sensitive to both internal feedback and external, environmental processes (e.g., Dekel & Silk 1986; Thoul & Weinberg 1996; Benson et al. 2002; Okamoto et al. 2010). This quality makes them excellent objects with which to study the effects of the surrounding environment and its role in dwarf galaxy physics. Previous studies have shown that dwarf galaxies are susceptible to quenching of their star formation through various processes including ram pressure stripping (e.g., the process of stripping of gas from an infalling satellite galaxy by the gaseous halo of the host galaxy; Grebel et al. 1926; van Gorkom 2004; Tonnesen & Bryan 2009), stellar feedback, and tidal stripping. Among these quenching mechanisms, ram pressure

Original content from this work may be used under the terms of the Creative Commons Attribution 4.0 licence. Any further distribution of this work must maintain attribution to the author(s) and the title of the work, journal citation and DOI.

stripping has been shown to be the primary mechanism of quenching in simulations (Murakami & Babul 1999; Mayer et al. 2006; Slater & Bell 2014; Kazantzidis et al. 2017; Simpson et al. 2018), while stellar feedback can increase the efficiency of ram pressure stripping by heating the gas reservoir (Bahé & McCarthy 2015; Kazantzidis et al. 2017). The ELVES III survey (Greene et al. 2023) has explored quenching fractions of quiescent and star-forming galaxies for 30 Local Volume hosts, finding that quenching fractions in these hosts are similar to that of the Milky Way and that the quenching time increase with stellar mass. Akins et al. (2021) found that galaxies with stellar masses $M_* \geqslant 10^8 \, M_\odot$ show resistance to environmental quenching.

To assess the effectiveness of ram pressure stripping, Taibi et al. (2022) examined metallicity gradients in galaxies as a potential signature of radially dependent environmental quenching. In particular, the gas content of a galaxy is expected to be directly linked to ram pressure stripping, whereas galaxies with lower gas content are more likely to have undergone this process. However, Taibi et al. (2022) found no correlation of metallicity gradient with internal gas content or distance from the host galaxy. Taibi et al. (2022) categorized their galaxy sample based on HI gas content but did not observe a statistically significant difference between gas-poor and gas-rich systems. These findings differ from the results reported by Leaman et al. (2013). In their study, gas-poor systems exhibited a radially decreasing metallicity profile, while gas-rich systems displayed a flat profile. Taibi et al. (2022) attribute this contradiction primarily to a difference in sample sizes. Their results suggest a limited role of environmental interactions with satellite galaxies in shaping their metallicity gradients. Although an increase in the scatter of metallicity gradients was observed, its statistical insignificance makes it challenging to confirm whether ram pressure (or tidal) stripping plays a significant role in influencing metallicity gradients. Given the sensitivity of dwarf galaxies to these quenching effects, it is important to understand how they affect dwarf galaxy properties such as their luminosities and their metal content, and how such effects depend on the environment and mass of the host halo.

While studies of dwarfs in the Local Group alone cannot give a clear picture of the role the environment plays in the physics of their evolution, several studies have now explored Milky Way-like galaxies in the Local Volume (Geha et al. 2017; Mao et al. 2021; Carlsten et al. 2022). Such observational studies of the Local Volume include the ELVES survey (Greene et al. 2023), and surveys of cluster scale environments such as Virgo $\sim 10^{15} M_{\odot}$ and Fornax $\sim 10^{14} M_{\odot}$ (Richardson et al. 2011; Ferrarese et al. 2012; McConnachie 2012; Eigenthaler et al. 2018). With the upcoming unprecedented volume of observations through soon-to-be available facilities such as the Nancy Grace Roman telescope and Rubin Observatory, it is essential that we explore dwarfs beyond the Local Group with theoretical models. One method of investigation is through the luminosity-metallicity relation, which is imprinted with the stellar feedback physics of dwarf galaxies. Studies have shown that the mass-metallicity relationships of both the Milky Way and M31 follow similar trends (Kirby et al. 2020). Thus, it is imperative that we look beyond the Local Group (LG) to understand whether or not properties in dwarf galaxies are independent of the environment, specifically the mass of their host halo.⁵

Centaurus A is the closest, easily observable giant elliptical galaxy located 3.8 Mpc from the Milky Way (Harris et al. 2010). It provides the most accessible opportunity to study dwarf galaxies within a higher mass host and in an environment that sits between group and cluster scales. The question of how dwarf galaxy physics is affected by different mass hosts needs further exploration in these intermediate mass host environments. In recent years the halo of Centaurus A has been targeted by several surveys including the Survey of Centaurus A's Baryonic Structures (SCABS; Taylor et al. 2016, 2017, 2018) and the Panoramic Imaging Survey of Centaurus & Sculptor (PISCeS; Crnojević et al. 2014, 2016; Sand et al. 2014). These are the first systematic surveys of the dwarf satellites of Centaurus A. In addition, studies by Müller et al. (2015, 2017, 2019, 2021, 2022) have also covered both M83 and Centaurus A with DECam. As a result of these surveys, the number of known or suspected dwarf galaxies has almost doubled over the past 5-10 yr.

The mass of Centaurus A is currently not well constrained. Several studies have attempted to estimate the virial mass of Centaurus A using a variety of methods. For example, Woodley et al. (2007) estimated the mass of Centaurus A (specifically the pressure-supported and rotational-supported mass) using the globular cluster population within 50 kpc (finding a mass of $1.3 \times 10^{12} M_{\odot}$). van den Bergh (2000) calculated the mass of Centaurus A using the virial theorem

 $(1.4\times10^{13}\,M_\odot)$ and the projected mass method out to 640 kpc $(1.8\times10^{13}\,M_\odot)$. Müller et al. (2022) estimates a dynamical mass of $1.2\times10^{13}\,M_\odot$ within 800 kpc. Pearson et al. (2022) have placed a lower limit (>4.7 × $10^{12}\,M_\odot$) on the mass of Centaurus A using stellar stream models. The upper range of virial masses measured for Centaurus A is $\sim10^{13}M_\odot$ (van den Bergh 2000; Peng et al. 2004; Woodley et al. 2007; Łokas 2008; Harris et al. 2015), which falls between the masses of Milky Way and large clusters such as Virgo and Fornax.

To date, however, few theoretical studies of the Centaurus A system have been carried out. Bovill et al. (2016) used a highresolution N-body simulation that did not include baryons to study the Centaurus A globular clusters, and Müller et al. (2019) compared the luminosity function within 200 kpc to Centaurus A analogs in the TNG100 simulation (Pillepich et al. 2018). However, hydrodynamical simulations of massive systems outside our Galactic neighborhood that have been run all the way to z = 0 do not meet the resolution required to fully resolve the star formation physics of fainter dwarfs. For example, TNG100 has a resolution of $m_{\rm DM} = 7.5 \times 10^6 \, M_{\odot}$ and $m_{\rm baryon} = 1.4 \times 10^6 \, M_{\odot}$ resolving galaxies with $M_* > 10^8 \, M_{\odot}$ (Pillepich et al. 2018). This is barely sufficient to resolve Small Magellanic Cloud analogs and is inadequate to resolve fainter dwarfs. Even the higher resolution TNG50 simulation (Nelson et al. 2019) can only resolve dwarf galaxies down to $M_* = 10^8 M_{\odot}$. Therefore, we need to explore more computationally efficient techniques, such as semianalytic models (SAMs) that provide an efficient method to explore the star formation physics of dwarf galaxies.

Our previous work modeling the satellites of the Milky Way (Weerasooriya et al. 2023) made use of the GALACTICUS SAM (Benson 2012) and demonstrated that it can be constrained to simultaneously and accurately reproduce the luminosity function and luminosity-metallicity relation of the Milky Way dwarfs, while also successfully reproducing the velocity dispersions, half-light radii, mass-to-light ratios, and star formation histories of dwarf galaxies down to and including the Sloan Digital Sky Survey (SDSS) ultrafaints. The key baryonic physics in this model includes reionization occurring at z = 9 (and subsequently heating the intergalactic medium, preventing accretion of gas into halos with virial velocities below 25 km s⁻¹), and star formation following the model of Blitz & Rosolowsky (2006). In our SAM, stellar feedback accounted for by assuming that stellar winds and supernovaedriven outflows remove gas from the interstellar medium of a galaxy, with this mass loss becoming inefficient in galaxies with circular velocities above approximately 150 km s⁻¹, and becoming more efficient in shallower potential wells. Both ram pressure and tidal stripping of baryons are also included. Full details of the model can be found in Weerasooriya et al. (2023) —we will also review key components of the model relevant to this work in Section 2.2. In this work, we run GALACTICUS on two different sets of halo merger trees: one generated using extended Press-Schechter (EPS) theory, and a second taken from an N-body simulation of a Centaurus A analog. We use the same astrophysical models (as described in detail in Weerasooriya et al. 2023 and briefly reviewed in Section 2.2) that reproduce the properties of observed dwarfs of the Milky Way down to ultrafaint dwarfs. The goal of this work is to test whether these same astrophysical prescriptions and parameters can reproduce the observed cumulative luminosity function and

To clarify terminology, we refer to the, typically low-mass, halo in which a satellite dwarf galaxy formed, and which it resides at the center of, as its "subhalo." We refer to the halo of the larger galaxy within which the dwarf satellite orbits as its "host halo."

the luminosity-metallicity relation of the Centaurus A satellites, and, if it can, make predictions for their properties and star formation histories (SFHs), in an effort to investigate the effects of host environment on these dwarfs.

The remainder of this paper is organized as follows. In Section 2, we describe the details of the *N*-body simulation of a Centaurus A analog and describe our semianalytic model, including the implementation of the EPS merger trees, galactic structure, and velocity dispersion. In Section 3, we describe the sample of observational data taken from the literature. Next, in Section 4, we compare our models to the observed properties of the known Centaurus A dwarfs before exploring their potential star formation histories. Lastly, we present our discussions and conclusions in Section 6.

2. Methods

2.1. N-body Simulation

To carry out of modeling of the Centaurus A system, we make use of a high-resolution cosmological zoom-in N-body simulation of an isolated Centaurus A halo from Bovill et al. (2016). To generate this simulation, first a cosmological simulation was run using a $100 h^{-1}$ Mpc periodic cube with $N = 256^3$ particles, allowing potential Centaurus A candidate halos to be resolved at z = 0 with over 1000 particles. This simulation was run from z = 150 to z = 0 with using the WMAP9 cosmology ($\sigma_8 = 0.821$, $H_0 = 70.0 \text{ km s}^{-1} \text{ Mpc}^{-1}$, $\Omega_b = 0.0463$, $\Omega_m = 0.279$, $\Omega_{\Lambda} = 0.721$). Initial conditions were generated using MUSIC (Hahn & Abel 2011) and the simulation was run with Gadget 2 (Springel 2005). Dark matter halos were identified in the simulation and their properties (including masses, Navarro-Frenk-White (NFW) scale radii, spin vectors, positions, and velocities) were calculated using the AMIGA halo finder (Knollmann & Knebe 2009). These halos were then linked through cosmic time to create merger trees using CONSISTENT TREES (Behroozi et al. 2013b).

From this set of halos, a Centaurus A analog was selected by seeking halos with mass $^6 \sim 10^{13}\,M_\odot$ that have no halos with mass greater than $10^{12}\,M_\odot$ within $3\,h^{-1}\,\mathrm{Mpc}$ at z=0. The Lagrangian region of this halo (corresponding to approximately 4 times the virial radius (2.4 Mpc) at z=0) was then resimulated to produce a higher resolution region that covers two times the virial radius at z=0 with no contamination by low-resolution particles. This resimulation was performed using an effective number of particles $N_{\rm eff}=8192^3$, corresponding to a particle mass of $m_{\rm p}=1.4\times10^5M_\odot$, using a force softening length of $\epsilon=200\,h^{-1}$ pc. This resolution ensures that halos of mass greater than $10^7\,M_\odot$ are resolved with at least 100 particles.

2.2. Semianalytic Model

We model the baryonic content of the Centaurus A system using the semianalytic model (SAM) GALACTICUS (Benson 2012). We applied the same astrophysical prescriptions and

parameters that we found were able to accurately reproduce the Milky Way satellites in Weerasooriya et al. (2023). That is, we assume that the underlying physics that determines dwarf galaxy formation is the same in both the Milky Way and Centaurus A systems.⁷

Of these astrophysical prescriptions, quenching due to ram pressure and tidal stripping primarily determine how dwarf satellites are affected by the environment of their host halo. For example, ram pressure stripping can strip gas out of dwarf galaxies resulting in a shortage of gas supply and eventual quenching of star formation. In Weerasooriya et al. (2023) we found that ram pressure stripping was ineffective at quenching Milky Way satellite galaxies, even when made as efficient as physically plausible. Regardless, in this work, we implement ram pressure stripping with the same high efficiency as in Weerasooriya et al. (2023).

As discussed in the Introduction, the virial mass of Centaurus A is highly uncertain. To explore the effects of this uncertainty on our model predictions we wish to investigate a range of possible halo masses for Centaurus A, consistent with the wide range of observational estimates. As we have only a single N-body realization of the Centaurus A halo, to explore a range of halo masses we make use of EPS (Press & Schechter 1974; Bond et al. 1991; Bower 1991; Lacey & Cole 1993) merger trees spanning the full range of possible Centaurus A halo masses $(5 \times 10^{12} M_{\odot})$ to $1 \times 10^{13} M_{\odot})$ and constructed using the algorithm of Parkinson et al. (2008; see also Cole et al. 2000) with a minimum resolved halo mass of $1.41 \times 10^7 M_{\odot}$ —corresponding to the lowest mass halos resolved in our high-resolution N-body simulation. Furthermore, we generate 30 realizations at each halo mass, allowing us to explore the halo-to-halo variations in the dwarf galaxy population. While these EPS trees allow us to efficiently probe a range of $M_{\rm vir}$ for the Centaurus A halo, they do not provide detailed positional information on the satellites. As such, EPS trees, unlike their N-body counterparts, do not allow us to explore the dependence of satellite populations on their distance from the host center. From this point onward we will refer to merger trees generated through the EPS method as "EPS trees" and the merger tree from the N-body simulation of Bovill et al. (2016) as an "N-body tree."

For a complete description of the GALACTICUS SAM we refer the reader to Benson (2012). However, in Subsections 2.2.1–2.2.3, we will briefly review key components of the model that are directly relevant to this work. We note that other than the determination of halo concentrations (see Section 2.2.1), all halo and galaxy physics is implemented and applied identically for *N*-body and EPS merger trees.

2.2.1. Galactic Structure

Each halo in a merger tree is considered a potential site of galaxy formation (if gas is able to accrete into and cool within the halo—see Weerasooriya et al. 2023). Each galaxy is approximated as consisting of one or both of a rotationally supported disk and a pressure-supported spheroid. Cooling gas initially settles into a disk, where it may form stars, but can later become part of the spheroid through the action of

⁶ As described in the Introduction, the mass of Centaurus A is poorly constrained observationally. Furthermore, the estimates that have been made (van den Bergh 2000; Peng et al. 2004; Woodley et al. 2007; Łokas 2008; Harris et al. 2015; Pearson et al. 2022) have adopted a variety of definitions of virial mass. Given the lack of strong constraints, we choose a value of $10^{13} M_{\odot}$, defined as the mass enclosed by a spherical region with density contrast appropriate to the spherical collapse model; Bryan & Norman (1998). We will adopt this same definition of virial mass throughout this work.

⁷ Of course, the prescriptions adopted in Weerasooriya et al. (2023) all have physically motivated scalings. For example, the effects of the ram pressure stripping scale in proportion to the square of the orbital velocity of each dwarf galaxy, and so will be greater in Centaurus A than in the Milky Way for any given dwarf.

dynamical instabilities in the disk or mergers with other galaxies.

To describe the density distribution of the system we model the dark matter halo as an NFW distribution (Navarro et al. 1997), adiabatically compressed by the gravitational potential of the disk and spheroid following the algorithm of Gnedin et al. (2004). In the case of *N*-body merger trees, the NFW scale radii of halos are measured by the CONSISTENTTREES code and are used directly in our calculations. For EPS trees we instead make use of the concentration–mass-redshift relation of Diemer & Joyce (2019) which was calibrated to accurately match the distribution of halo concentrations measured in *N*-body simulations. In this model the concentration of a halo is given by:

$$c = C(\alpha_{\text{eff}}) \times \tilde{G}\left(\frac{A(n_{\text{eff}})}{\nu}\left[1 + \frac{\nu^2}{B(n_{\text{eff}})}\right]\right),$$
 (1)

where

$$n_{\text{eff}}(M) = \frac{d \log P(k)}{d \log k} \bigg|_{k = \kappa 2\pi/R_L}, \tag{2}$$

 $R_{\rm L}$ is the Lagrangian radius of a halo of mass M, P(k) is the linear-theory power spectrum as a function of wavenumber k, $\nu = \delta_{\rm c}/\sigma(M)$ is the peak-height parameter, $\delta_{\rm c} \approx 1.686$ is the critical overdensity for the collapse of a spherical top-hat perturbation, $\sigma(M)$ is the fractional root variance of the density field in spheres containing, on average, a mass M, $A(n_{\rm eff}) = a_0[1+a_1(n_{\rm eff}+3])$, $B(n_{\rm eff}) = b_0[1+b_1(n_{\rm eff}+3])$, $C(\alpha_{\rm eff}) = 1-c_\alpha(1-\alpha_{\rm eff})$, and \tilde{G} is the inverse of $G(x) = x/g(x)^{(5+n_{\rm eff})/6}$, with $g(x) = \log(1+x) - x/(1+x)$. For the constants κ , a_0 , a_1 , b_0 , and b_1 we take the best-fit values found by Diemer & Joyce (2019).

This fitting function gives the concentration of a halo for the case where the virial radius is defined as that radius that encloses a mean density of 200 times the critical density of the Universe. Using the NFW profile, we convert this to the corresponding concentration under our preferred definition of the virial radius. Wang et al. (2020; their Figure 3) compare the predictions of the Diemer & Joyce (2019) concentration—mass relation to the results of N-body simulations down to very low halo masses. For masses above $10^7 M_{\odot}$ (the lowest halo mass considered in this work), the Diemer & Joyce (2019) fitting function is accurate to better than 0.05 dex.

Galaxy disks are modeled as vertically thin, exponential disks. The radial scale length of each disk is found by requiring that the disk be rotationally supported in the combined gravitational potential of the dark matter halo, disk, and spheroid. To do this we follow the general approach of Cole et al. (2000). Briefly, we first compute the specific angular momentum of the disk. Angular momentum is supplied to the disk when gas from the circumgalactic medium (CGM) cools and inflows into the disk—the specific angular momentum of CGM gas is assumed to be comparable to that of the dark matter halo, and to be conserved as the gas flows into the disk. Angular momentum is also lost from the disk due to outflows and transport of disk material into the spheroid. Full details can be found in Benson (2012), Weerasooriya et al. (2023), and Ahvazi et al. (2024). Once the specific angular momentum of the disk is known, we solve for a scale radius, $r_{\rm d}$ which

satisfies:

$$r_{\rm d}[V_{\rm d}^2(r_{\rm d}) + V_{\rm s}^2(r_{\rm d}) + \tilde{V}_{\rm h}^2(r_{\rm d})]^{1/2} = j_{\rm d},$$
 (3)

where $j_{\rm d}$ is the specific angular momentum of the disk at its scale radius (assuming a flat rotation curve), and $V_{\rm d}(r)$, $V_{\rm s}(r)$, and $\tilde{V}_{\rm h}(r)$ are the rotation curves due to the disk, spheroid, and adiabatically contracted halo respectively.

Spheroids are modeled as Hernquist (1990) profiles. The scale radius of this profile is found using a similar approach as for the disk. Even though the spheroid is pressure supported, we compute a pseudospecific angular momentum—essentially the specific angular momentum that the spheroid would have if it were rotationally supported. We then solve for the scale radius in the same way as described above for the disk, but using this pseudospecific angular momentum. Full details of this approach are given in Cole et al. (2000). As these rotational support calculations must take into account the self-gravity of disk and spheroid components (and because of the inclusion of adiabatic contraction of the dark matter halo), the above equations are solved using an iterative method at each evolution step in our SAM.

2.2.2. Line-of-sight Velocity Dispersion

Given the structure of a halo+galaxy system as computed in Section 2.2.1 we can estimate a line-of-sight velocity dispersion for the spheroid component. To do so we assume that the spheroid is in the Jeans equilibrium (with an isotropic velocity distribution) in the combined gravitational potential of the adiabatically contracted halo, disk, and its own self-gravity. For dwarf galaxies, the gravitational potential is largely dominated by the contribution of their dark matter subhalo. Cole & Lacey (1996) have shown that the Jeans equilibrium provides an accurate description of the velocity dispersion as a function of radius measured for N-body dark matter halos. We first solve for the 1D velocity dispersion as a function of radius, $\sigma(r)$, in the spheroid by integrating the Jeans equation from infinity to each radius. Then, to estimate an observable velocity dispersion, we compute the density-weighted line-of-sight velocity dispersion at the half-mass-radius, $r_{1/2}$, of the Hernquist profile for each spheroid:

$$\sigma_{\log}^2 = \int_{r_{1/2}}^{\infty} \sigma^2(r) \rho(r) \frac{r}{\sqrt{r^2 - r_{1/2}^2}} dr / \int_{r_{1/2}}^{\infty} \rho(r) \frac{r}{\sqrt{r^2 - r_{1/2}^2}} dr,$$
(4)

where $\rho(r)$ is the Hernquist profile of the spheroid.

2.2.3. Spectra and Magnitudes

Weerasooriya et al. (2023) describe in detail how we model star formation in our model. Once the star formation rate as a function of time, $\phi(t)$, in a galaxy disk or spheroid is known we compute the stellar spectrum of that component as:

$$F(\lambda) = \int_0^t \phi(t') S(\lambda | t - t', Z[t]) dt', \tag{5}$$

where Z[t] is the metallicity of stars forming at time t, and $S(\lambda|\tau, Z)$ is the spectrum of a unit mass, single age, single metallicity stellar population of age τ and metallicity Z. For $S(\lambda|\tau, Z)$ we adopt the models of Conroy et al. (2009; as implemented by Conroy & Gunn 2010) assuming a Chabrier (2001) initial mass function.

Table 1
Properties of Galaxies in the Centaurus A System

Name	R.A. _h (hr)	R.A. _m (minutes)	R.A. _s (s)	Decl. _{deg} (deg)	Decl. _{arcmin} (arcmin)	Decl. _s (arcsec)	M _B (mag)	M_r (mag)	M_V (mag)	Distance (Mpc)	References
NGC 4945	13	5	26.1	-49	28	16.0	-20.34	-18.2	-20.6	3.47	(1, 7)
NGC 5102	13	21	57.8	-36	37	47.0	-18.24	-20.13	-20.37	3.66	(1, 7)
E383-087	13	49	17.5	-36	3	48.4	-16.83	-17.17	-17.31	3.19	(1, 7)
NGC 5206	13	30	41.0	-47	53	42.0	-16.43	-16.97	-16.90	3.6	(1, 7)
NGC 5408	14	0	18.0	-41	8	11.0	-15.91	-16.27	-17.3	4.81	(2, 7)
E324-24	13	27	37.4	-41	28	50.0	-15.49	-15.41	-15.6	3.78	(2, 7)
E26958	13	7	38.0	-46	43	30.0	-14.99	-17.09	-16.8	3.63	(6, 7)
NGC 5237	13	37	38.9	-42	50	51.0	-14.82	-15.27	-15.08	3.33	(3, 5, 7)
NGC 5011C	13	13	11.9	-43	15	56.0	-14.15	-14.19	-15.8	3.73	(2, 3, 7)
E325-11	13	45	0.8	-41	51	32.0	-14.02	-14.47	-14.5	3.4	(3, 6, 7)

Note. Column (1) gives the name of each galaxy, columns (2)–(4) show R.A., columns (5)–(7) decl., columns (8)–(10) B-, r-, and V-band absolute magnitude respectively, column (11) gives distance, and column (12) lists the references from which this information was drawn.

References. (1) Lauberts & Valentijn (1989), (2) de Vaucouleurs et al. (1991), (3) Karachentsev et al. (2003), (4) James et al. (2004), (5) Doyle et al. (2005), (6) Sharina et al. (2008), (7) Karachentsev et al. (2013), (8) Müller et al. (2015), (9) Müller et al. (2017), (10) Crnojević et al. (2014, 2016, 2019), (11) Taylor et al. (2018). (This table is available in its entirety in machine-readable form.)

Observed luminosities in any band of interest⁸ are then found by integrating this spectrum under the appropriate filter response curve. This allows us to find the luminosity of the disk and spheroid component of each galaxy in a band of interest. Given these, the structural properties of disk and spheroid (found as described in Section 2.2.1), and the assumption that the starlight in each component follows the same radial distribution as the mass (i.e., an exponential disk and a Hernquist 1990 spheroid) we can numerically solve for the half-light radius of each galaxy in any band of interest.

3. Observational Sample

Observations of the Centaurus A dwarfs are inhomogeneous, therefore in this section we describe the sample of Centaurus A dwarfs taken from the literature that we will compare to our models. We use observational data for Centaurus A satellites from a variety of sources including Crnojević et al. (2010, 2014, 2016, 2019), Karachentsev et al. (2013), Müller et al. (2015, 2017, 2019), Taylor et al. (2016, 2018), which are presented in Table 1. In addition to the dwarfs in the above sample, we also include 38 new dwarf galaxy candidates from M. Taylor (2024, in preparation) in our overall analysis, but do not list their properties in Table 1. This new sample includes only those galaxies with distance or velocity measurements that verify them as members of Centaurus A with distances ≤5.8 Mpc.

Absolute magnitudes of observed Centaurus A dwarfs are reported in a variety of different bands. To facilitate some comparisons with our model, we convert these observations to a common band, for which we choose the V band. To perform this conversion, consider an observed galaxy with a reported absolute magnitude in the "X" band (where "X" here can be any observed band) of M_X . We compute the median V-X color of Centaurus A dwarfs from observations, $\overline{M_V-M_X}$, including all Centaurus A dwarfs with absolute magnitudes measured in both the V and X bands. We then approximate the V-band absolute magnitude of the observed dwarf as $M_V \approx M_X + \overline{M_V-M_X}$. Any galaxy lacking an observed V-band magnitude, but with observed magnitude in some other band X is converted

to V-band magnitudes in this way. We apply this conversion only to dwarfs lacking V-band magnitude data in the literature, and only for Figures 1 and 2. In other figures, we show only those dwarfs for which measured V-band magnitudes are available in the literature.

The current sample of observations of Centaurus A is incomplete due to three major reasons: (1) Lack of systematic sky coverage that leads to spatial incompleteness. For example, the PISCeS survey is spatially incomplete and biased toward coverage of the Northeastern region of Centaurus A's halo. These nonuniformities in design or analysis make completeness calculations more complex. (2) The detectability limits of different surveys, e.g., SCABS is limited to $M_V < -7.2$ within 150 kpc covering an area of 50 square degrees and surface brightness limit of 27.8 mag $arcsec^{-2}$ in the g band (C. D. Leahy et al. 2024, private communication), while PISCeS can detect dwarfs down to $M_V < -8$ within 150 kpc and with a surface brightness limit of 26.5 mag $arcsec^{-2}$ in the g band (Crnojević et al. 2014, 2019). (3) The lack of distance measurements in the outskirts also hinders the determination of membership (Müller et al. 2017; Taylor et al. 2018). Distances are essential to determine the membership of satellites, their shape, and their brightness. Thus larger uncertainties in distances can cause these data to have larger uncertainties in their sizes and magnitude measurements. However, the observational sample is relatively complete within 200 kpc (Müller et al. 2019) down to $M_V = -10$. The SCABS and PISCeS surveys cover a spatial region within a projected radius of 150 kpc down to dwarfs as faint as $M_V < -7.2$ (Crnojević et al. 2014, 2016; Taylor et al.2016).

Under the definition adopted in this work, and assuming a mass of $10^{13} M_{\odot}$ for the halo of Centaurus A, the corresponding virial radius is 562 kpc (somewhat larger than the estimate of ~409 kpc from Tully 2015, but comparable given the large uncertainties in the halo mass). However, it is expected that many satellites of Centaurus A will be found beyond this radius, yet within Centaurus A's "splashback radius." The splashback radius is a physically motivated halo boundary that eliminates spurious evolution of radius and mass caused by standard definitions of virial radius (Diemer & Kravtsov 2014; Deason et al. 2020; Shin & Diemer 2023). We estimate the splashback radius of Centaurus A using the model of

 $^{^8\,}$ In this work we will consider the standard V band, along with the SDSS g band, and DES g band.

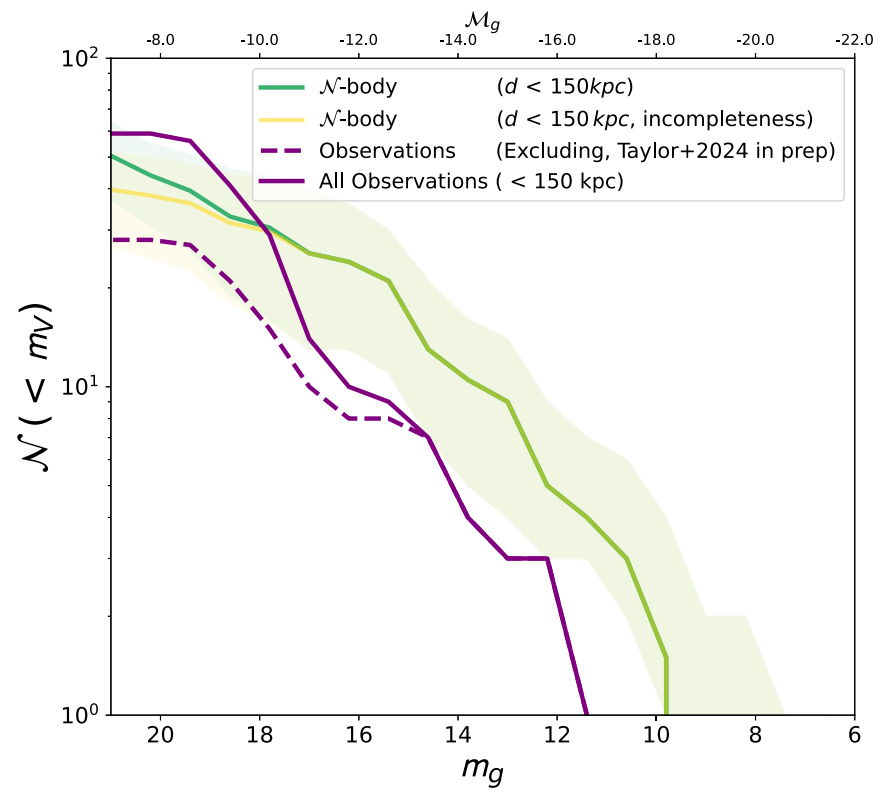


Figure 1. The cumulative, *V*-band luminosity function as a function of apparent magnitude within a projected distance of 150 kpc of Centaurus A, corresponding to the region which is well covered by the SCABS and PISCeS surveys. The *y*-axis shows the number of galaxies brighter than a given *V*-band apparent magnitude. For reference, the corresponding absolute magnitude at the distance of Centaurus A is shown on the upper axis. The solid purple curve shows all known observed galaxies, including those from SCABS (including the SCABS dwarfs from M. Taylor 2024, in preparation) and PISCeS. The dashed purple curve excludes new dwarfs from the sample of M. Taylor (2024, in preparation). Predictions from our model, using our *N*-body merger tree, are indicated by the green curve and shaded regions, which represent the median and full extent over all viewing angles. The yellow curve shows the same model results, but accounting for the observational completeness fractions as calculated by C. D. Leahy et al. (2024, private communication).

Diemer (2020), which predicts⁹ a splashback radius of 712 kpc. Therefore we will also consider model predictions within a projected radius of 700 kpc to approximately capture the entirety of the satellite population within this splashback radius. While current observations are highly incomplete in this region—limiting any comparison between model and observations—our results serve as testable predictions for future observational campaigns.

The observational properties of Centaurus A satellites are still largely unknown. Thus our knowledge of these galaxies and their properties is nowhere near as complete as our knowledge of the Milky Way system. Quantitative estimates of the incompleteness of Centaurus A dwarfs have not been made by previous studies, and such exploration is beyond the scope of our current work. A preliminary quantitative exploration of the completeness limits in SCABS Centaurus A satellites is underway by C. D. Leahy et al. (2024, private communication). These completeness tests are preliminary results based on artificial galaxy experiments using an automated dwarf galaxy selection technique. These results are based on an analysis in the g'band and are applied to a small subset of the overall SCABS imaging that does not extend beyond 150 kpc. Their exploration of completeness using 5000 Monte Carlo dwarf galaxy realizations reveals completeness of 96% for dwarf

galaxies of \lesssim 18 mag in the g band. They report 50% completeness at g-band magnitudes of 20.01 and 50% completeness at surface brightness of ~ 27.8 mag arcsec⁻². In Figure 1, we compare our models within 150 kpc to the total number of galaxies expected in the region based on these preliminary artificial galaxy experiments. While this region only covers a fraction of the entire virial volume of Centaurus A, it provides an almost complete observational census of dwarfs with which to compare our model. Note that, as we must select model galaxies based on their projected position relative to the center of their host halo, we show results only for our model applied to the N-body simulation, for which such positions are available. The green curve shows the number of satellites predicted within 150 kpc of Centaurus A, and the yellow curve shows the same model with the incompletenesses of C. D. Leahy et al. (private communication) applied to that model. This curve signifies the number of satellites predicted by the model within 150 kpc that would be observable. As there is no preferred viewing angle of our modeled Centaurus A, we rotate the model distribution of galaxies around the \hat{z} -axis of the simulation in 5° steps, project the galaxy positions into the y-z plane, and repeat the projected radius selection at each step. This provides an estimate of the uncertainty in the predicted luminosity function due to the anisotropy of the system. This error envelope is indicated by the shaded region. The purple curves show the observed dwarfs within 150 kpc of Centaurus A, with the solid line showing all observations and the dashed line excluding the dwarfs of M.

⁹ Diemer (2020) show that the splashback radius depends on a halo's accretion rate. Lacking any knowledge of the accretion rate of Centaurus A's halo we adopt the mean value for halos of its mass, also computed using the model of Diemer (2020).

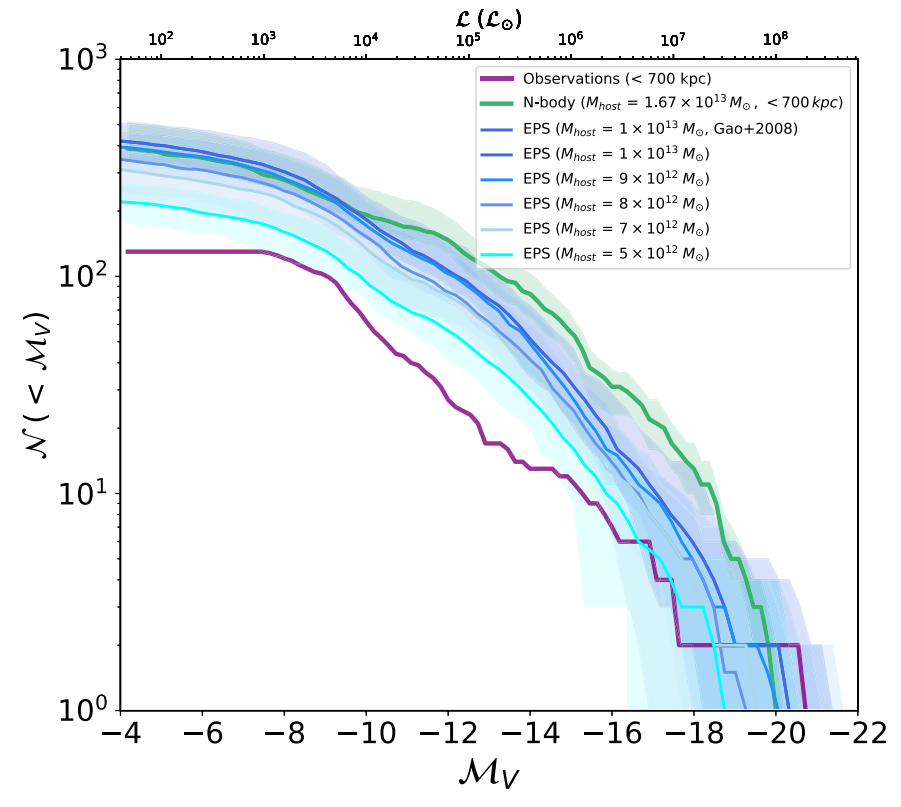


Figure 2. Luminosity functions for the Centaurus A satellites within 700 kpc projected radius (around 1.5 times the virial radius, and corresponding to the likely splashback radius of Centaurus A) for models and observations. The purple line shows the observational sample. The predicted luminosity functions for Centaurus A satellites with $M_V \leqslant -4$ from our *N*-body merger tree are shown in green, while lines shown in shades of blue represent EPS trees with different Centaurus A masses as indicated in the figure. Each blue line shows the median luminosity function over 30 different EPS trees, with the shaded region indicating the minimum and maximum.

Taylor (2024, in preparation). We note here that given the unconfirmed natures of the M. Taylor (2024, in preparation) dwarf candidates, this estimate should be considered as an upper limit with results interpreted in that context. Based on the comparison, our galaxy models agree with the observed luminosity function, although the observed luminosity function demonstrates a slightly steeper slope within this 150 kpc radius. Nevertheless, the lower boundary of the luminosity function envelope that accounts for different projections along the line of sight generated from the *N*-body model is consistent with observations for the fainter dwarfs (see also Figure 3). At brighter magnitudes ($M_V < -14$), our model predicts marginally more galaxies than are observed. This is consistent with other studies of the inner 200 kpc of the Centaurus A halo (Müller et al.2019).

We reiterate that the observational knowledge of the dwarf galaxy population of Centaurus A beyond 150 kpc remains highly incomplete and the completeness of the galaxy sample in these outer regions is not well characterized. In much of the remainder of this work we will present model predictions throughout the entirety of the Centaurus A system (out to the splashback radius). These should be viewed as testable predictions for future observational campaigns.

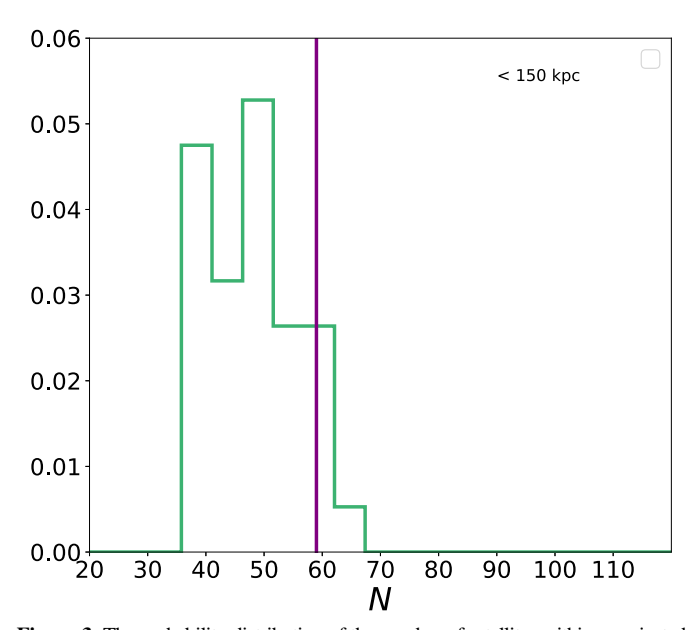


Figure 3. The probability distribution of the number of satellites within a projected distance of 150 kpc of Centaurus A and brighter than $M_V \le -6$ for different lines of sight as the model is rotated in the y–z plane (green histogram). The mean and median of this distribution are 48.1 and 49 respectively. The purple line shows the total number of satellites in the observed sample (59).

4. Properties of Centaurus A Dwarfs

In this section, we compare different properties of the modeled Centaurus A dwarfs with observational data described in Section 3. We start by exploring the properties of the

The galaxies beyond the regions surveyed by SCABS and PISCeS are drawn from a variety of different literature sources. Completeness estimates are not available for any of these samples and, in most cases, even the area of sky surveyed is unclear, making any correction for incompleteness and survey area impossible.

Centaurus A dwarfs including luminosities, half-light radii, and velocity dispersions.

4.1. Luminosity Function

In Figure 2, we plot the cumulative luminosity function of Centaurus A satellites for observations within a projected radius of 700 kpc—approximately 1.5 times the virial radius and consistent with the likely splashback radius of Centaurus A. Selection of model galaxies based on projected radius is possible only when using *N*-body trees, for which positional information is available. The median luminosity function over all potential viewing angles is shown in green, while the maximum and minimum are shown by the shaded envelope. All observations are converted to *V*-band magnitudes as described in Section 3.

We also run models using merger trees generated via an EPS approach to explore the mass range of Centaurus A's halo. EPS models for different mass merger trees—spanning the plausible range of masses for the Centaurus A halo—are shown in shades of blue. These models inherently do not have positional information. However, by construction, all galaxies in the EPS trees are within the splashback radius. Therefore we include all the galaxies in merger trees for these models. The solid curves show the median per $M_{\rm V}$ bin with shaded areas indicating the minimum and maximum over 30 EPS trees. All of these models follow the general shape of the luminosity function for observations within 700 kpc. However, there is some variation in the shape of the luminosity functions between N-body and EPS merger trees.

The purple line in Figure 2 shows the cumulative luminosity function of known, observed satellite galaxies within 700 kpc of Centaurus A. As discussed in Section 3 the observed sample of galaxies in this region is likely to be highly incomplete—more so at faint magnitudes—and no good estimates of completeness (or the fraction of the projected area of the Centaurus A system surveyed to a given depth) are available. As such, the purple line in Figure 2 should be considered to be a lower limit to the true luminosity function, particularly at fainter magnitudes.

While we cannot constrain the mass of Centaurus A from the models due to poorly understood completeness in the observations for fainter dwarfs, comparison with models at the bright end of the luminosity function suggests that Centaurus A is likely to have a higher mass $(10^{13}\,M_\odot)$. Our model is consistent with the overall shape of the observed cumulative luminosity function for both *N*-body and EPS merger trees at all modeled host masses.

The poorly understood completeness limits of the observations within 700 kpc of Centaurus A make exploration of these satellites and their properties limited (see Section 3 for a detailed discussion of completeness). In Figure 3 we show the distribution of the number of bright ($M_V \le -6$) satellites within a projected distance of 150 kpc of Centaurus A (for which observations *are* largely complete to this magnitude) in our model as the line of sight is rotated relative to the \hat{z} direction in 5° increments as the green histogram. For comparison we show the number of observed satellites of the same brightness in this region as a vertical purple line. Our model predicts a median of 49 which is lower than the observed number of dwarf galaxies (59) located within 150 kpc of Centaurus A, but the observed number is well within the distribution predicted by our model. Perhaps surprisingly, the brightest observed satellites of the

Centaurus A system (which extend to magnitudes of around $M_V = -21$ as shown in Figure 2) are not found within 150 kpc of Centaurus A. As such, they do not appear in Figure 1 which includes only this inner region. While these very luminous galaxies are not considered dwarfs, and so their spatial distribution is not directly relevant to the focus of this paper, we note that our N-body simulation never predicts zero such galaxies in this region. ¹¹

4.2. Half-light Radii

In Figure 4, we compare the half-light radii versus luminosity for the modeled dwarfs (using the *N*-body merger tree in the right panel and 30 EPS merger trees with $\sim 1 \times 10^{13}\,M_{\odot}$ in the left panel) with the observed Centaurus A dwarfs (Crnojević et al. 2016, 2019; M. Taylor 2024, in preparation) along with observations of other systems such as the Milky Way, and M31 (McConnachie 2012) for comparison. We note that the majority of observations beyond the Local Group are not sensitive to surface brightnesses below $0.01\,L_{\odot}\,\mathrm{pc}^{-2}$.

At high luminosities, the modeled sizes of the dwarfs agree with observations of the Centaurus A dwarfs. However, the modeled sizes for the fainter dwarfs are larger than the observed values. This is consistent with the systematically larger sizes of the fainter-modeled dwarfs compared to observations of the Milky Way satellites (Weerasooriya et al. 2023). GALACTICUS tends to overpredict the half-light radii with merger trees generated from EPS and *N*-body simulations. EPS trees lose accuracy for halos with $\leq 10^{10} M_{\odot}$ due to dynamic range limitations (Somerville & Kolatt 1999; Zhang et al. 2008). This may lead to inaccuracies in halo masses and/ or formation times, which may subsequently affect the sizes of the galaxies forming in these halos. N-body trees over estimate half-light radii if a halo has N < 1000 particles (Weerasooriya et al. 2023). A more detailed investigation of how the resolution affects the size of the modeled dwarfs will be a subject of future study.

4.3. Metallicity

Currently available observed metallicities of Centaurus A dwarfs are limited in number. In Figure 5 we show the observations of [Fe/H] for Centaurus A satellites from Crnojević et al. (2010, 2014, 2019) and Müller et al. (2019, 2021). Notice that Müller et al. (2019) find a [Fe/H] ~ -2.25 metallicity floor between $M_V \sim -8$ and -10. However, their measurement errors are ~0.5 dex, making the observations consistent with our modeled values. While spectroscopic measurements of metallicities by Müller et al. (2021) agree well with Milky Way dwarfs, their photometric measurements are reported to have a larger scatter. The authors state that the scatter might be due to the age-metallicity degeneracy and incorrect assumptions of uniformly old (~10 Gyr) stellar populations. Using the same astrophysical prescriptions and parameters as those that reproduced the luminosity-metallicity relations of the Milky Way dwarfs, we present the modeled metallicities of the Centaurus A dwarfs in 1 30 $M_{\rm vir} = 10^{13} M_{\odot}$ EPS trees and for satellites within 700 kpc for the N-body tree. The metallicities of the modeled dwarfs in

 $[\]overline{^{11}}$ Of course, our *N*-body simulation is just a single realization and so we cannot draw strong conclusions from this apparent discrepancy with the observations.

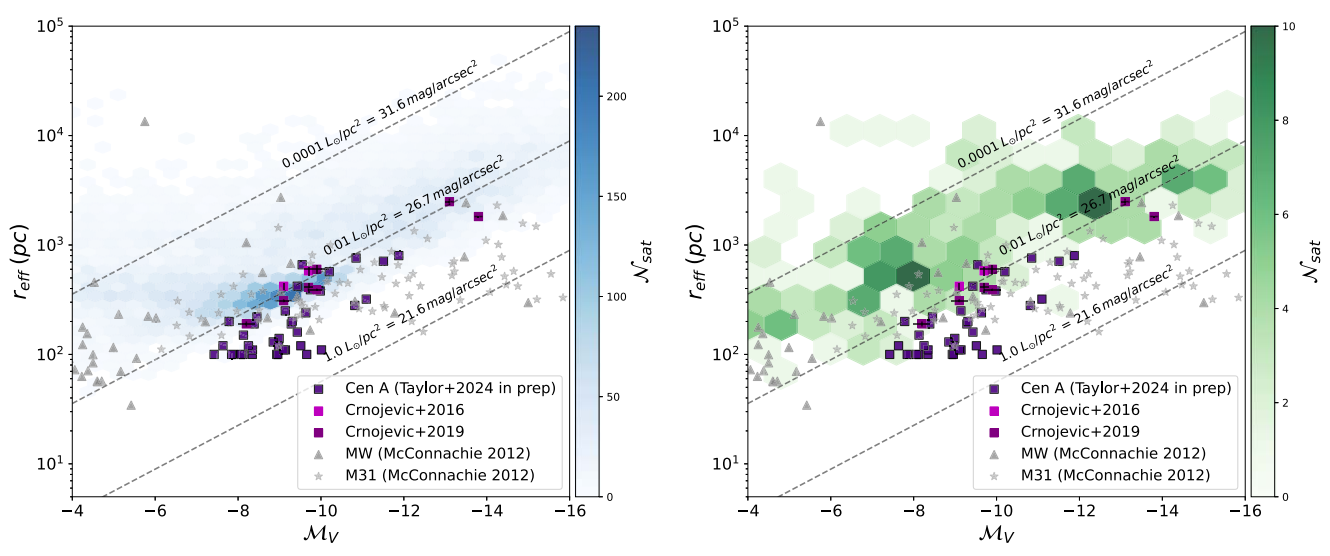


Figure 4. Half-light radii vs. the absolute *V*-band magnitude of the Centaurus A satellites are shown for both modeled and observed galaxies. The left panel shows the distribution of model results using EPS merger trees (blue hexagons), while the right panel shows the distribution of model results using the *N*-body merger tree within a projected distance of 700 kpc in order to encompass all satellites within the backsplash volume (green hexagons). The contrast of each hexagon indicates the number of model galaxies falling within that region, as indicated by the color bar to the right of each panel. For model galaxies, half-light radii are measured in the g_{DES} band, although the dependence of half-light radius on the band is quite small. The same observational data is repeated in each panel. Specifically, we show observed half-light radii of Centaurus A dwarfs (measured in the g_{DES} band; M. Taylor 2024, in preparation) as dark purple squares, and Crnojević et al. (2016, 2019; *V* band) as magenta squares. The observations of McConnachie (2012) for the Milky Way (measured in the *V* band), and M31 (measured in the *V* band) are also shown as gray triangles and stars respectively. Iso-surface brightness lines are shown as gray dashed lines. The predicted trend for half-light radii is consistent with that which our model predicted for the Milky Way satellites (Weerasooriya et al. 2023).

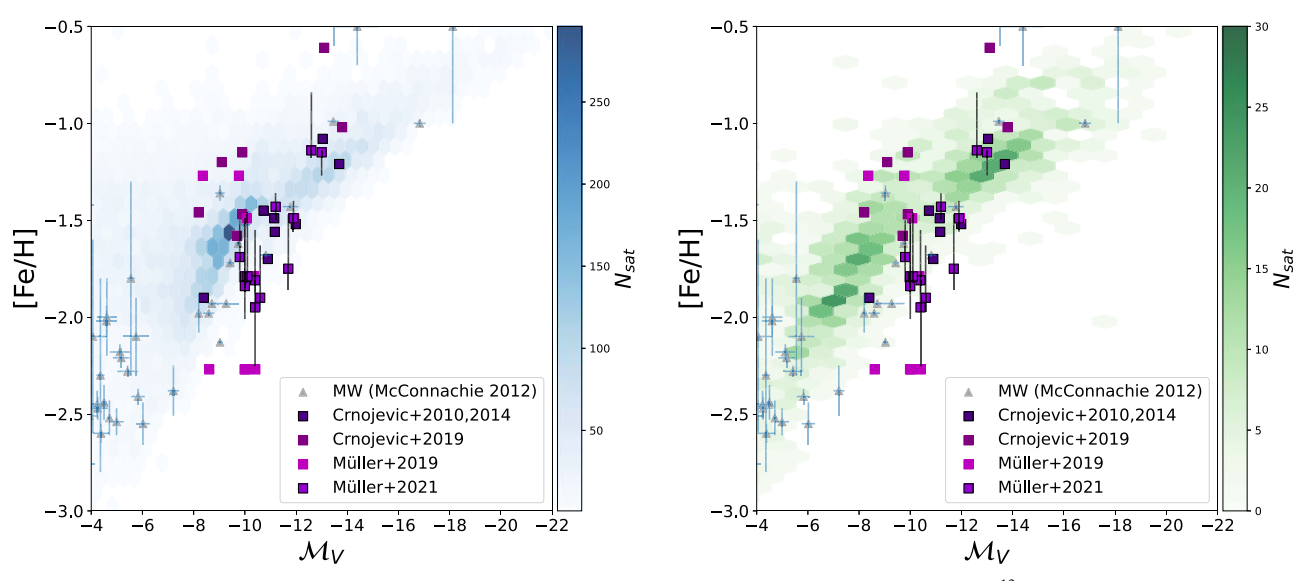


Figure 5. The luminosity-metallicity relation predicted for the Centaurus A satellites using 30 EPS trees with mass $10^{13}M_{\odot}$ (left panel) and N-body trees with satellites within a projected distance of 700 kpc in order to encompass all satellites within the backsplash volume (right panel). The contrast of each hexagon indicates the number of model galaxies falling within that region, as indicated by the color bar to the right of each panel. Observed values are shown by squares (Crnojević et al. 2010, 2019; Müller et al. 2019, 2021). The metallicities of the Milky Way satellites are shown as gray triangles (McConnachie 2012). The same observed data are reproduced in each panel.

this work agree well with currently available observations of Centaurus A satellites (Crnojević et al. 2010, 2019; Müller et al. 2019). This could potentially mean that the Centaurus A satellites have a similar enrichment history to that of the Milky Way's satellites and/or that dwarf metallicities are independent of their local environment. In Weerasooriya et al. (2023), we show that ram pressure does not significantly affect the luminosity–metallicity relation of the Milky Way satellites. We therefore do not expect a significant change in luminosity–metallicity relation as a function of halo mass. Furthermore,

models run with and without ram pressure stripping effects result in very similar luminosity-metallicity relations for the modeled dwarf satellites of Centaurus A.

4.4. Velocity Dispersion

The velocity dispersion of the stars in a satellite galaxy is largely determined by the gravitational potential of the subhalo in which they live—therefore, velocity dispersions are a sensitive probe of the masses and gravitational potentials of

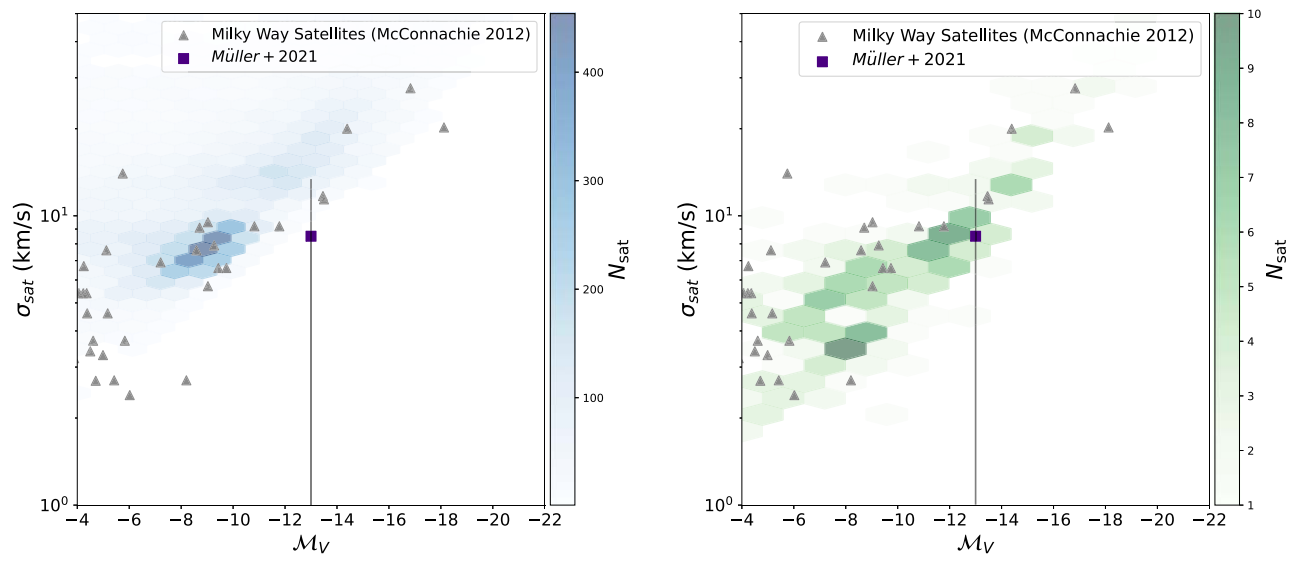


Figure 6. The relation between line-of-sight stellar velocity dispersion (computed at the stellar half-mass-radius of each galaxy) and *V*-band absolute magnitude in Centaurus A galaxies. We show results for EPS merger trees (left panel) and *N*-body merger trees (right panel) as blue and green hexagons respectively. For the *N*-body tree, we show all satellites within a projected distance of 700 kpc in order to encompass all satellites within the backsplash volume. The contrast of each hexagon represents the number of model galaxies found within that region, as indicated by the color bar to the right of each panel. Gray triangles show the observed velocity dispersions of the Milky Way satellites (McConnachie 2012). The purple square indicates the measured velocity dispersion of Centaurus A satellite galaxy KK197 (Müller et al. 2021). The same observational data are reproduced in both panels. Note that the predicted values of Centaurus A satellites are consistent with the velocity dispersion of the observed Milky Way satellites.

those subhalos (Wake et al. 2012; Bogdán & Goulding 2015; Schechter 2015). However, velocity dispersions of Centaurus A satellites are unknown with the exception of KK197. As such, additional data is required before any comparison can be made to the population as a whole. In Figure 6, we show the velocity dispersion of KK197 (Müller et al. 2021), and those of the Milky Way satellites (McConnachie 2012). We calculate the velocity dispersion (σ_{sat}) at stellar half-mass radii for the modeled dwarfs. As described in detail in Section 2.2.2, we assume the Jeans equilibrium in the total gravitational potential (i.e., self-gravity and the gravitational potential of the dark matter halo) when calculating the velocity dispersion of stars as a function of radius $\sigma(r)$. This $\sigma(r)$ is then integrated along the line of sight at the half-mass-radius, weighted by the luminosity profile of the galaxy to predict the observed velocity dispersion. Most of our modeled sample falls within the observed velocity dispersions of the Milky Way satellites (McConnachie 2012). Given that velocity dispersion probes dark matter subhalo mass, this suggests that Centaurus A dwarfs occupy similar halos, at a given luminosity/stellar mass, as their Milky Way counterparts.

5. Star Formation Histories

Detailed star formation histories of Centaurus A dwarfs have not yet been measured observationally. In fact, only a few measurements of the present-day star formation rates of Centaurus A dwarfs exist: star formation rates of KK197, ESO-269066, ESO-381018 (Makarova et al. 2007) and five dwarf irregulars KK182 (Cen6), ESO269-58, KK196 (AM1318-444), HIPASS J1348-37, ESO384-16 (Crnojević et al. 2012) are available in literature. Both KK197 and ESO-269066 are dwarf spheroidals, while ESO-269066 is a dwarf irregular galaxy. Dwarf spheroidals typically have old stellar populations whose light is dominated by their red giant branches, while dwarf irregulars are metal poor and have varying levels of current star formation. Crnojević et al. (2012)

state that KK197 and ESO-269066 have unusual RGB color scatter, which shows active star formation with high metallicity, while ESO-381018 is a typical dwarf irregular. Two of the dwarf irregulars (KK196 and ESO269-58) studied are within 700 kpc of Centaurus A (see Figure 6 of Crnojević et al. 2012). Positioned in the middle of Centaurus A's southern radio lobe, KK196 has a star formation rate of $0.0046 \pm 0.0004 M_{\odot} \,\mathrm{yr}^{-1}$ and has formed more than $60\%^{+20\%}_{-30\%}$ of its stars more than 5 Gyr ago ($\tau_{60} = 5$ Gyr;¹² Crnojević et al. 2012). Meanwhile, ESO269-58, located $300 \pm 50 \, \text{kpc}$ from Centaurus A, has few blue loops, red supergiants, very broad red giant branch stars, and a dense asymptotic giant branch zone. This dwarf has a higher star formation rate compared to KK196 with $0.07 \pm 0.04 \, M_{\odot} \, \text{yr}^{-1}$, and has formed $50\%_{-15\%}^{+15\%}$ of stars more than 5 Gyrs ago($\tau_{50} = 5$ Gyr). While its star formation activity has been enhanced between 3 and 5 Gyr ago, Crnojević et al. (2012) also find that Centaurus A has lowered its star formation rate in the last 1 Gyr.

In this section we provide predictions for these SFHs from our model, along with distributions of quenching times (which we will define below). We remind the reader that the physical prescriptions that determine SFHs (cooling in the circumgalactic medium, star formation rates, feedback models, and ram pressure stripping) are identical to those used by Weerasooriya et al. (2023), who demonstrated that these prescriptions could successfully reproduce the SFHs of Milky Way dwarf satellites. We therefore explore the predictions of these prescriptions—which contain the relevant physical scalings to allow them to be extended to the Centaurus A environment—which may be used to test our model against future observational determinations of SFHs.

In addition to full SFHs, we can also infer quenching times—a measure of when the star formation in a galaxy ended.

 $[\]overline{^{12}}$ We define τ_X as the lookback time at which a galaxy had formed X% of its final stellar mass.

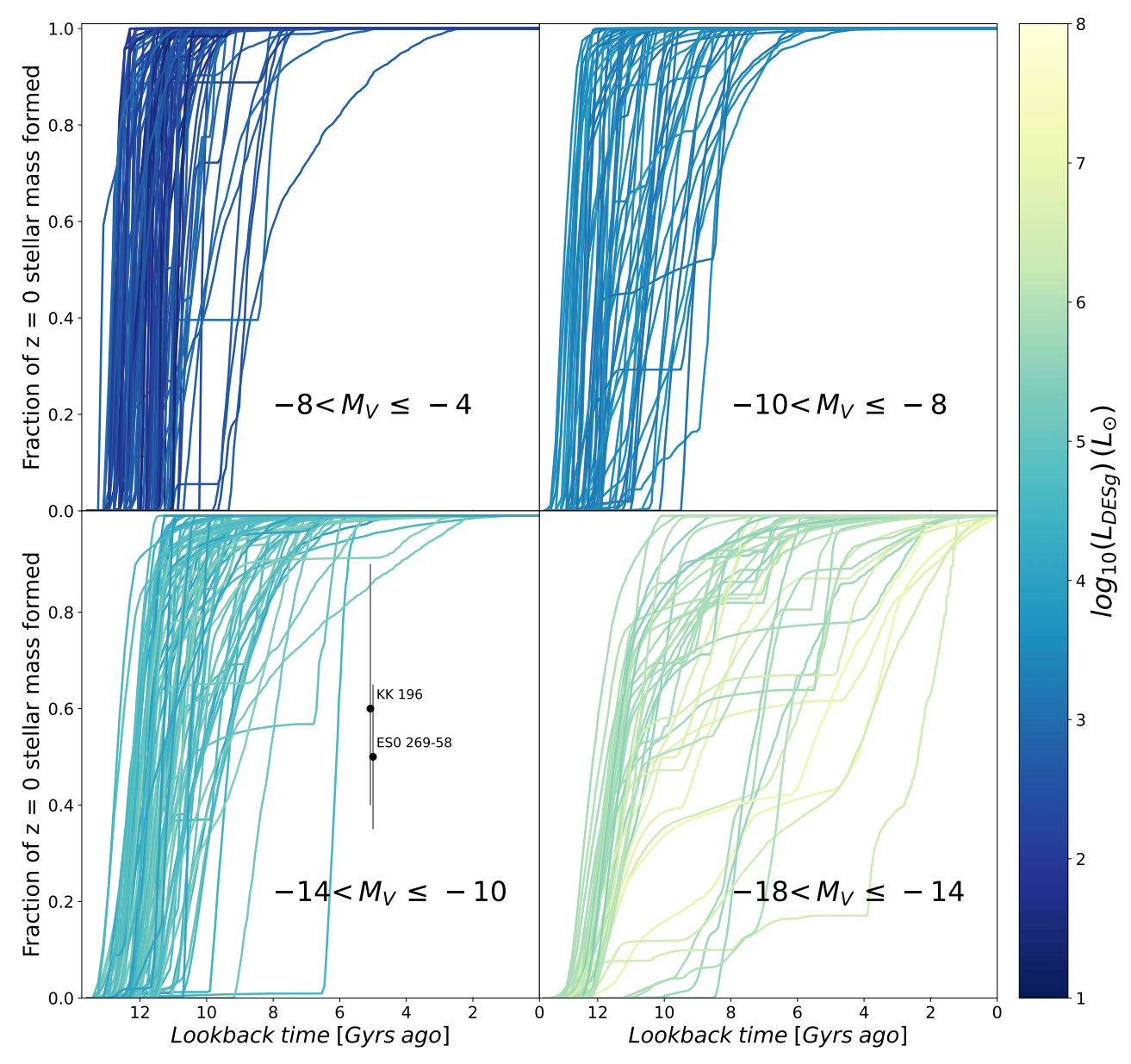


Figure 7. Cumulative star formation histories are shown for Centaurus A satellites within 700 kpc projected distance from the center of the host halo as predicted by our model using our *N*-body merger tree. The cumulative fraction of stars formed is shown as a function of lookback time. Individual SFHs are colored by their luminosity in the g_{DES} band as indicated by the color bar on the right of the figure. Galaxies are divided into four panels based on their absolute magnitudes: $-8 < M_V \le -4$, $-10 < M_V \le -8$, $-14 < M_V \le -10$, and $-18 < M_V \le -14$ as indicated in each panel. In the lower-left panel, the two available observational measurements are shown as black circles with error bars.

Quenching times have been quantified in a variety of different ways in the literature. Most commonly, the quenching time has been defined as the period for which a satellite remains star forming after infall into its host halo (Rocha et al. 2012; Weisz et al. 2015; Foltz et al. 2018). Other studies define quenching time as the time at which the specific star formation rate falls below 10^{-11} yr⁻¹ (Akins et al. 2021) or use both (Baxter et al. 2022). However, in this work, we choose to use the time at which a galaxy had formed 90% of its present-day stellar mass, τ_{90} , as our definition of quenching time. This has the advantage of being observationally measurable—in Weerasooriya et al. (2023) we demonstrated that our model produced distributions of τ_{90} broadly consistent with those measured by Weisz et al. (2019) for Milky Way dwarf satellites. The distributions of τ_{90} for Centaurus A dwarfs will serve as a testable prediction of our model that can be confirmed, or refuted, by future observations.

In Figure 7, we show the modeled cumulative star formation histories of the Centaurus A satellites as a function of lookback time colored by their absolute V-band magnitude at z=0 from our N-body merger tree. As expected, our Centaurus A modeled SFHs are similar to those of the Milky Way satellites in Weerasooriya et al. (2023), indicating no strong influence of the host halo environment on the SFHs.

In the upper left panel, we show the faintest dwarfs with $-8 < M_V \le -4$. Most of these ultrafaint dwarfs quenched 8–12 Gyrs ago—this is similar to ultrafaints around the Milky Way which are fossils of the first galaxies (Bovill & Ricotti 2011; Brown et al. 2012). While such faint galaxies have not yet been observed in the Centaurus A system, it is expected that observations will reach these magnitudes in the next generation of surveys. Experiments by Mutlu-Pakdil et al. (2021) show that LSST could detect Centaurus A dwarfs down

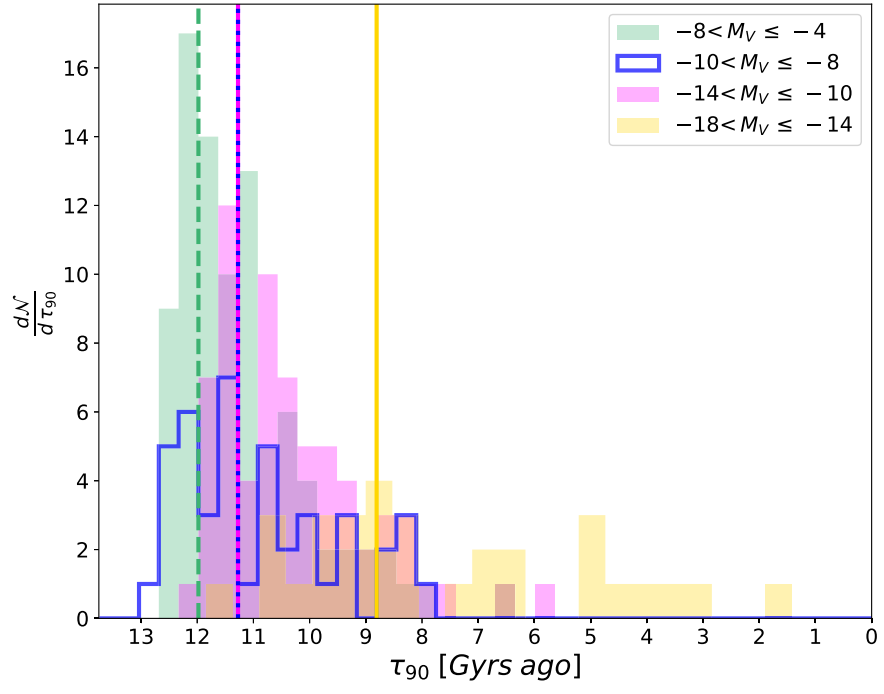


Figure 8. The distributions of quenching times (τ_{90} , the lookback time at which a particular galaxy has formed 90% of its stellar mass at z=0) for the panels shown in Figure 7. The faintest satellites quenched around 12 Gyrs ago, while satellites between $-14 \le M_V \le -8$ quenched after 11.2 Gyrs ago. The most luminous galaxies quench much later \sim 8.8 Gyrs ago. Median values for each distribution are shown by vertical lines.

to $M_V \leqslant -7$. Furthermore, simulations based on extrapolations of HST observations indicate that the Nancy Grace Roman Space Telescope will be able to resolve stellar populations in M83 which is at a distance of 4.5 Mpc, even further than Centaurus A (Akeson et al. 2019).

The upper-right and lower-left panels show satellites in the range $-10 < M_V \leqslant -8$ and $-14 < M_V \leqslant -10$ respectively. The majority of these satellites quenched 10–12 Gyrs ago, with a small fraction quenching later (6–10 Gyr ago). The two measured τ_X values for observed Centaurus A dwarfs discussed earlier fall in the magnitude range of the lower-left panel of Figure 7, and are indicated by black circles with error bars. Our model predicts higher stellar mass fractions formed by these times than the observations suggest, although the uncertainties in the measurements remain large. The brightest galaxies $(-18 < M_V \leqslant -14)$, shown in the lower right panel, show noticeably more extended SFHs. This is clearly seen in Figure 8 which shows the corresponding distributions of τ_{90} for the same four intervals of absolute magnitude.

6. Summary and Conclusions

We have presented predictions for the properties of the dwarf galaxy population orbiting the Centaurus A galaxy, using our semianalytic model GALACTICUS applied to merger trees produced from both an *N*-body simulation and from the application of EPS theory. This model was previously calibrated to match the observed properties of Milky Way dwarf galaxies (Weerasooriya et al. 2023), and we retain the same calibration here, allowing us to make testable predictions for the Centaurus A system. Importantly, the astrophysics models controlling key baryonic processes (e.g., star formation, feedback, and ram pressure stripping) incorporate the expected scalings of these processes with host halo mass and environment. As such, the predictions of our model for the dwarf population of the Centaurus A system can be seen as a potential

test of the underlying physics. We find that our model is able to reproduce the overall properties of the Centaurus A dwarf population quite well, given the sparse nature of the current observations.

In particular, we find that our model is able to correctly reproduce the number of dwarf galaxies found within a projected radius of 150 kpc of Centaurus A (the region for which observational surveys are reasonably complete), although it predicts somewhat more of the brightest satellite galaxies than are observed in this inner region. Expanding to the full extent of the Centaurus A system (i.e., out to the expected splashback radius of the system at around 700 kpc) we find that our model is in good agreement with the number of known highly luminous satellites. This suggests that the excess of bright satellite galaxies in the inner 150 kpc region predicted by our model may simply be a result of random fluctuations in galaxy positions, as we have only a single N-body realization of this system. Further testing of this hypothesis is planned using additional N-body simulations, and the more detailed orbital model of satellite galaxies employed by Ahvazi et al. (2024). At fainter luminosities, our model predicts between 200 and 500 satellites brighter than $M_M = -4$ within the backsplash radius. Compared to the approximately 120 known dwarfs (down to the current detection threshold of $M_M = -8$) this suggests that many hundreds of dwarf satellites remain to be discovered around Centaurus A.

In addition to these global properties, we have also explored predictions for internal properties of Centaurus A dwarfs. We find that our model predicts half-light radii of these dwarfs which are in good agreement with observations for brighter $(M_M < -10)$ dwarfs, but overpredicts sizes of fainter systems. A similar conclusion was reached for Milky Way dwarfs by Weerasooriya et al. (2023), who suggest that this may be due to the limited resolution of the associated *N*-body halos, and inaccuracy in the EPS approach for lower halo masses.

We find that our model predicts metallicities as a function of luminosity that are consistent with observations in the Centaurus A system. Given that, in our model, the metallicity attained by a galaxy is largely driven by the process of stellar feedback (which ejects gas and metals from galaxies), and halo assembly history, this suggests that our models of these processes are consistent with observations. Furthermore, we find that the metallicity-luminosity ratio of model dwarfs in the Centaurus A system is consistent with that predicted for the Milky Way dwarfs by Weerasooriya et al. (2023). This implies that environmental processes (such as ram pressure stripping), which may affect metal enrichment in our model, are subdominant to internal processes (star formation and feedback). To further test this hypothesis we have repeated our model calculations without the effects of ram pressure stripping, finding almost no change in the predicted metallicity-luminosity relation, consistent with the conclusions of the observational analysis of Taibi et al. (2022).

Predicted line-of-sight velocity dispersions of model galaxies as a function of luminosity are also found to be consistent with those found by Weerasooriya et al. (2023) for Milky Way dwarfs. As velocity dispersion in dwarfs is largely determined by the depth of the gravitational potential well of the dwarf's subhalo, this implies that dwarfs of a given luminosity form in subhalos of approximately the same mass independent of environment. The single measured velocity dispersion in the Centaurus A system (for dwarf galaxy KK197) is consistent with our model predictions (although the measurement is highly uncertain).

Finally, we have also explored predictions for the star formation histories (SFHs) of Centaurus A dwarfs, characterizing these by the cumulative mass fraction of stars formed as a function of lookback time, and by the summary statistic τ_{90} (the lookback time at which 90% of the final stellar mass had formed). Once again, our results closely resemble those predicted for Milky Way dwarfs by Weerasooriya et al. (2023; which were themselves consistent with observational estimates of SFHs in those systems), also indicating that internal processes are dominant in guiding the formation of these dwarf galaxies. Observational measures of star formation histories exist for only two Centaurus A dwarfs presently. While these measurements are highly uncertain, they suggest star formation is delayed relative to the predictions from our model. Future measurements may, therefore, be able to strongly test and rule out the specific star formation model adopted in this work.

Dwarf galaxies, with their shallow potential wells and large numbers, are uniquely well suited to testing models of feedback and environmental effects in galaxy formation. Given the large theoretical uncertainties in these processes, comparing models to observations across a range of environments can provide a strong and useful test of whether internal or external processes are responsible for shaping the evolution of these galaxies. Using our current model, presented in Weerasooriya et al. (2023), this work shows that internal processes (star formation and feedback) seem to be the dominant drivers of dwarf galaxy evolution. While the current observations in the Centaurus A system are largely consistent with our predictions, the limited number and precision of these observations do not currently provide strong tests of this model. However, there are hints of tensions between theory and observations (for example, in the histories of star formation in more luminous dwarfs). The next

generation of galaxy surveys (to be carried out by facilities such as the Rubin Observatory and Nancy Grace Roman Space Telescope) have the potential to dramatically increase both the size and precision of observational samples. The predictions presented in this work are likely to be strongly testable in the near future.

Acknowledgments

We thank the anonymous referee for their valuable feedback and insightful suggestions, which have significantly enhanced the quality of this manuscript. The authors acknowledge the University of Maryland supercomputing resources (http://hpcc.umd.edu) made available for conducting the research reported in this paper. All EPS trees used in this paper were conducted via the Resnick High Performance Computing Center, a facility supported by Resnick Sustainability Institute at the California Institute of Technology.

Software: GALACTICUS (Benson 2011), ROCKSTAR (Behroozi et al. 2013a), AMIGA (Knollmann & Knebe 2009), CONSISTENT_TREES (Behroozi et al. 2013b), JUPYTER (Kluyver et al. 2016), NUMPY (Harris et al. 2020), SCIPY (Virtanen et al. 2020), and MATPLOTLIB (Hunter 2007).

ORCID iDs

Sachi Weerasooriya https://orcid.org/0000-0001-9485-6536 Mia Sauda Bovill https://orcid.org/0000-0003-4037-5360 Andrew J. Benson https://orcid.org/0000-0001-5501-6008 Cameron Leahy https://orcid.org/0000-0002-0091-9610

References

```
Abbott, T. M. C., Abdalla, F. B., Alarcon, A., et al. 2018, PhRvD, 98, 043526
Aguado, D. S., Ahumada, R., Almeida, A., et al. 2019, ApJS, 240, 23
Ahvazi, N., Benson, A., Sales, L. V., et al. 2024, MNRAS, 529, 3387
Akeson, R., Armus, L., Bachelet, E., et al. 2019, arXiv:1902.05569
Akins, H. B., Christensen, C. R., Brooks, A. M., et al. 2021, ApJ, 909, 139
Albareti, F. D., Allende Prieto, C., Almeida, A., et al. 2017, ApJS, 233, 25
Applebaum, E., Brooks, A. M., Christensen, C. R., et al. 2021, ApJ, 906, 96
Bahé, Y. M., & McCarthy, I. G. 2015, MNRAS, 447, 969
Baxter, D. C., Cooper, M. C., Balogh, M. L., et al. 2022, MNRAS, 515, 5479
Behroozi, P. S., Wechsler, R. H., & Wu, H.-Y. 2013a, ApJ, 762, 109
Behroozi, P. S., Wechsler, R. H., Wu, H.-Y., et al. 2013b, ApJ, 763, 18
Benson, A., 2011 Galacticus: A Semi-Analytic Model of Galaxy Formation,
   Astrophysics Source Code Library, ascl:1108.004
Benson, A. J. 2012, NewA, 17, 175
Benson, A. J., Lacey, C. G., Baugh, C. M., Cole, S., & Frenk, C. S. 2002,
  MNRAS, 333, 156
Binggeli, B., Sandage, A., & Tammann, G. A. 1988, ARA&A, 26, 509
Blitz, L., & Rosolowsky, E. 2006, ApJ, 650, 933
Bogdán, Á., & Goulding, A. D. 2015, ApJ, 800, 124
Bond, J. R., Cole, S., Efstathiou, G., & Kaiser, N. 1991, ApJ, 379, 440
Bovill, M. S., Puzia, T. H., Ricotti, M., & Taylor, M. A. 2016, ApJ, 832, 88
Bovill, M. S., & Ricotti, M. 2011, ApJ, 741, 17
Bower, R. G. 1991, MNRAS, 248, 332
Brown, T. M., Tumlinson, J., Geha, M., et al. 2012, ApJL, 753, L21
Bryan, G. L., & Norman, M. L. 1998, ApJ, 495, 80
Carlsten, S. G., Greene, J. E., Beaton, R. L., Danieli, S., & Greco, J. P. 2022,
    ApJ, 933, 47
Chabrier, G. 2001, ApJ, 554, 1274
Cole, S., & Lacey, C. 1996, MNRAS, 281, 716
Cole, S., Lacey, C. G., Baugh, C. M., & Frenk, C. S. 2000, MNRAS, 319, 168
Conroy, C., & Gunn, J. E., 2010 FSPS: Flexible Stellar Population Synthesis,
   Astrophysics Source Code Library, ascl:1010.043
Conroy, C., Gunn, J. E., & White, M. 2009, ApJ, 699, 486
Crnojević, D., Caldwell, N., Guhathakurta, P., et al. 2016, HST Proposal Cycle
Crnojević, D., Grebel, E. K., & Cole, A. A. 2012, A&A, 541, A131
Crnojević, D., Grebel, E. K., & Koch, A. 2010, A&A, 516, A85
Crnojević, D., Sand, D. J., Bennet, P., et al. 2019, ApJ, 872, 80
```

```
Crnojević, D., Sand, D. J., Caldwell, N., et al. 2014, ApJL, 795, L35
de Vaucouleurs, G., de Vaucouleurs, A., Corwin, H. G. J., et al. 1991, Third
   Reference Catalogue of Bright Galaxies (New York: Springer)
Deason, A. J., Fattahi, A., Frenk, C. S., et al. 2020, MNRAS, 496, 3929
Dekel, A., & Silk, J. 1986, ApJ, 303, 39
Diemer, B. 2020, ApJS, 251, 17
Diemer, B., & Joyce, M. 2019, ApJ, 871, 168
Diemer, B., & Kravtsov, A. V. 2014, ApJ, 789, 1
Doyle, M. T., Drinkwater, M. J., Rohde, D. J., et al. 2005, MNRAS, 361, 34
Eigenthaler, P., Puzia, T. H., Taylor, M. A., et al. 2018, ApJ, 855, 142
Ferguson, H. C., & Binggeli, B. 1994, A&ARv, 6, 67
Ferrarese, L., Côté, P., Cuillandre, J.-C., et al. 2012, ApJS, 200, 4
Foltz, R., Wilson, G., Muzzin, A., et al. 2018, ApJ, 866, 136
Geha, M., Wechsler, R. H., Mao, Y.-Y., et al. 2017, ApJ, 847, 4
Gnedin, O. Y., Kravtsov, A. V., Klypin, A. A., & Nagai, D. 2004, ApJ, 616, 16
Grebel, E. K., Gallagher, J. S. I., & Harbeck, D. 1926, AJ, 125, 1926
Greene, J. E., Danieli, S., Carlsten, S., et al. 2023, ApJ, 949, 94
Hahn, O., & Abel, T. 2011, MNRAS, 415, 2101
Harris, C. R., Millman, K. J., van der Walt, S. J., et al. 2020, Natur, 585, 357
Harris, G. L. H., Rejkuba, M., & Harris, W. E. 2010, PASA, 27, 457
Harris, W. E., Harris, G. L., & Hudson, M. J. 2015, ApJ, 806, 36
Hernquist, L. 1990, ApJ, 356, 359
Hopkins, P. F., Wetzel, A., Kereš, D., et al. 2018, MNRAS, 480, 800
Hunter, J. D. 2007, CSE, 9, 90
James, P. A., Shane, N. S., Beckman, J. E., et al. 2004, A&A, 414, 23
Karachentsev, I. D., Makarov, D. I., & Kaisina, E. I. 2013, AJ, 145, 101
Karachentsev, I. D., Makarov, D. I., Sharina, M. E., et al. 2003, A&A, 398, 479
Kazantzidis, S., Mayer, L., Callegari, S., Dotti, M., & Moustakas, L.A. 2017,
   ApJL, 836, L13
Kirby, E. N., Gilbert, K. M., Escala, I., et al. 2020, AJ, 159, 46
Kluyver, T., Ragan-Kelley, B., Pérez, F., et al. 2016, in Jupyter Notebooks—a
   publishing format for reproducible computational workflows, ed.
   F. Loizides & B. Scmidt (Amsterdam: IOS Press), 87
Knollmann, S. R., & Knebe, A. 2009, ApJS, 182, 608
Lacey, C., & Cole, S. 1993, MNRAS, 262, 627
Lauberts, A., & Valentijn, E. A. 1989, The Surface Photometry Catalogue of
  the ESO-Uppsala Galaxies (Garching: ESO)
Leaman, R., Venn, K. A., Brooks, A. M., et al. 2013, ApJ, 767, 131
Łokas, E. L. 2008, ApJL, 680, L101
Makarova, L., Makarov, D., Dolphin, A., et al. 2007, in IAU Symp. 235,
   Galaxy Evolution across the Hubble Time, ed. F. Combes & J. Palouš
   (Cambridge: Cambridge Univ. Press), 320
Mao, Y.-Y., Geha, M., Wechsler, R. H., et al. 2021, ApJ, 907, 85
Martin, N. F., Ibata, R. A., Lewis, G. F., et al. 2016, ApJ, 833, 167
Marzke, R. O., & da Costa, L. N. 1997, AJ, 113, 185
Mayer, L., Mastropietro, C., Wadsley, J., Stadel, J., & Moore, B. 2006,
   MNRAS, 369, 1021
McConnachie, A. W. 2012, AJ, 144, 4
Müller, O., Fahrion, K., Rejkuba, M., et al. 2021, A&A, 645, A92
```

Müller, O., Jerjen, H., & Binggeli, B. 2015, A&A, 583, A79

```
Müller, O., Jerjen, H., & Binggeli, B. 2017, A&A, 597, A7
Müller, O., Lelli, F., Famaey, B., et al. 2022, A&A, 662, A57
Müller, O., Rejkuba, M., Pawlowski, M. S., et al. 2019, A&A, 629, A18
Murakami, I., & Babul, A. 1999, MNRAS, 309, 161
Mutlu-Pakdil, B., Sand, D. J., Crnojević, D., et al. 2021, ApJ, 918, 88
Navarro, J. F., Frenk, C. S., & White, S. D. M. 1997, ApJ, 490, 493
Nelson, D., Pillepich, A., Springel, V., et al. 2019, MNRAS, 490, 3234
Okamoto, T., Frenk, C. S., Jenkins, A., & Theuns, T. 2010, MNRAS,
  406, 208
Pandya, V., Somerville, R. S., Anglés-Alcázar, D., et al. 2020, ApJ, 905, 4
Parkinson, H., Cole, S., & Helly, J. 2008, MNRAS, 383, 557
Pearson, S., Price-Whelan, A. M., Hogg, D. W., et al. 2022, ApJ, 941, 19
Peng, E. W., Ford, H. C., & Freeman, K. C. 2004, ApJ, 602, 705
Pillepich, A., Nelson, D., Hernquist, L., et al. 2018, MNRAS, 475, 648
Press, W. H., & Schechter, P. 1974, ApJ, 187, 425
Richardson, J. C., Irwin, M. J., McConnachie, A. W., et al. 2011, ApJ, 732, 76
Rocha, M., Peter, A. H. G., & Bullock, J. 2012, MNRAS, 425, 231
Sand, D. J., Crnojević, D., Strader, J., et al. 2014, ApJL, 793, L7
Schechter, P. L. 2015, in IAU Symp. 317, The General Assembly of Halos, ed.
   A. Bragaglia arXiv:1508.02358
Sharina, M. E., Karachentsev, I. D., Dolphin, A. E., et al. 2008, MNRAS,
  384, 1544
Shin, T.-h., & Diemer, B. 2023, MNRAS, 521, 5570
Shipp, N., Panithanpaisal, N., Necib, L., et al. 2023, ApJ, 949, 44
Simpson, C. M., Grand, R. J. J., Gómez, F. A., et al. 2018, MNRAS, 478, 548
Slater, C. T., & Bell, E. F. 2014, ApJ, 792, 141
Somerville, R. S., & Kolatt, T. S. 1999, MNRAS, 305, 1
Springel, V. 2005, MNRAS, 364, 1105
Taibi, S., Battaglia, G., Leaman, R., et al. 2022, A&A, 665, A92
Taylor, M. A., Eigenthaler, P., Puzia, T. H., et al. 2018, ApJL, 867, L15
Taylor, M. A., Muñoz, R. P., Puzia, T. H., et al. 2016, arXiv:1608.07285
Taylor, M. A., Puzia, T. H., Muñoz, R. P., et al. 2017, MNRAS, 469, 3444
Thoul, A. A., & Weinberg, D. H. 1996, ApJ, 465, 608
Tonnesen, S., & Bryan, G. L. 2009, ApJ, 694, 789
Tully, R. B. 2015, AJ, 149, 54
van den Bergh, S. 2000, The Galaxies of the Local Group, 35 (Cambridge:
  Cambridge Univ. Press)
van Gorkom, J. H. 2004, in CGPC Symp., Clusters of Galaxies: Probes of
  Cosmological Structure and Galaxy Evolution, ed. J. S. Mulchaey,
   A. Dressler, & A. Oemler (Cambridge: Cambridge Univ. Press), 305
Virtanen, P., Gommers, R., Oliphant, T. E., et al. 2020, NatMe, 17, 261
Wake, D. A., van Dokkum, P. G., & Franx, M. 2012, ApJ, 751, 2
Wang, J., Bose, S., Frenk, C. S., et al. 2020, Natur, 585, 39
Weerasooriya, S., Bovill, M. S., Benson, A., Musick, A. M., & Ricotti, M.
  2023, ApJ, 948, 87
Weisz, D. R., Dolphin, A. E., Skillman, E. D., et al. 2015, ApJ, 804, 136
Weisz, D. R., Martin, N. F., Dolphin, A. E., et al. 2019, ApJL, 885, L8
```